Intelligently Wireless Batteryless RF-Powered Reconfigurable Surface: Theory, Implementation & Limitations

Iosif Vardakis*, Georgios Kotridis*, Spyridon Peppas*, Konstantinos Skyvalakis, Georgios Vougioukas and Aggelos Bletsas
School of Electrical and Computer Engineering, Technical University of Crete, Chania 73100, Greece
{ivardakis, gkotridis, speppas, kskyvalakis, gevougioukas}@isc.tuc.gr, aggelos@telecom.tuc.gr

***Abstract*—This work exploits ultra-low cost, commodity, radio frequency identification (RFID) tags as elements of a reconfigurable intelligent surface (RIS). Such batteryless tags are powered and controlled by a software-defined radio reader, with properly modified software, so that a source-destination link is assisted, operating at a different band. Signal model includes small-scale and large-scale fading, direct link, as well as specific parameters relevant to reflection (i.e., backscatter) radio, such as antenna structural mode and reflection efficiency, typically overlooked in the literature. An algorithm is offered that computes the optimal RIS configuration with complexity of $O(M \log M)$ in number of elements M, instead of intractable exponential complexity of exhaustive search, while accommodating any number $K \geq 2$ of loads. With the proposed algorithm, it is shown that performance gains reach a plateau for constant element spacing and increasing number of elements, suggesting that the weak, passive nature of backscattered links limits the performance gains, even with perfect channel estimation. Channel estimation with linear minimum mean squared error (LMMSE) estimator is shown to be effective, provided that there are sufficient number of pilot symbols. A concrete way is offered to design and prototype a wireless, batteryless, RF-powered, reconfigurable surface and a proof-of-concept is experimentally demonstrated.**

***Index Terms*—Backscatter Radio, RFID, Gen2, Reconfigurable Surface.**

I. Introduction

Significant interest has been attracted recently on reconfigurable intelligent surfaces (RISs), which are viewed as a way to control the environment, with a large number of passive elements, i.e., without amplification; such surfaces are envisioned to offer a *focusing* effect (e.g., review work in [1], [2], and references therein). Despite the fact that RIS is a special case of bistatic backscatter radio [3]–[5], or multistatic scatter radio [6], [7], such connection is not widely known in the literature. Backscatter, i.e., *reflection* radio has been extensively used in radio frequency identification (RFID) and recently was proposed for sensor networking applications (e.g., work in [8] for monostatic interrogation and work in [9]–[15] for bistatic, batteryless sensor interrogation and references therein). Review material and connection to ambient backscatter communication [16], a special case of bistatic backscatter, can be found in [17] and references therein.

*Equal contributors. Parts of this work were presented in IEEE GLOBECOM, Dec. 2021, Madrid, Spain. The research work was supported by the Hellenic Foundation for Research and Innovation (H.F.R.I.) under the "First Call for H.F.R.I. Research Projects to support Faculty members and Researchers and the Procurement of High-cost research equipment" (Project #: 2846).

A. Related Studies

According to [18], a near-field, squared-shaped RIS can offer limited gains. Firstly, given a large surface, the distance between the source and the elements of RIS can be much greater than the link distance (i.e. distance from source to the center of RIS), resulting in significant attenuation. Secondly, distant elements of the surface exhibit lower local effective areas. Finally, the polarization mismatch increases for the elements deployed far away from the center of the surface. Similarly, authors in [19], pinpoint that the received power scattered by a RIS is bounded as the size of the surface increases.

Assuming the presence of a RIS, work in [20] considered the joint maximization of spectral and energy efficiency in a multi-user MISO downlink network; alternative optimization of base station beamforming and RIS phase shifts was employed, subject to individual link budget guarantees for the mobile users. Such formulation led to non-convex optimization problems, addressed by two computationally affordable methods. In order to make the problem more tractable, the authors assumed infinite-resolution phase shifters, no direct links and perfect channel state information (CSI) available at the base station; comparison to multi-antenna amplify-and-forward relaying was also performed. In [21], the performance of a single-cell multiuser system aided by multiple RISs was evaluated. Through simulations, it was shown that the RIS-aided system can outperform full-duplex relaying, in terms of spatial throughput, when the number of RIS elements exceeds a certain value. Differently from the single-user case where the RIS should be deployed near the BS or user for rate maximization, RISs (in the multi-user system) should be distributed across the whole network.

Work in [22] introduced expressions to compute the power reflected from a RIS as a function of distance between the transmitter or receiver and the RIS, the size of the RIS and the phase transformation applied by RIS. Calculations were based on the general scalar theory of diffraction and the Huygens-Fresnel principle. Free space path loss models were offered in [23], along with an experimental testbed for their verification. It is noted that a significant issue on RIS implementation is the mutual coupling. Conceptually, each element modifies the phase of the impinging EM wave. When the elements are spaced by at least half of the wavelength, mutual coupling among them is usually ignored and each element can be

designed independently of the others [24].

Work in [25] employed tools from stochastic geometry and studied the effect of large-scale deployment of RISs on the performance of cellular networks. Direct links assumed blocked and blockages, such as buildings or trees, were modeled with a line Boolean model. A subset of the blockages was equipped with RISs and a performance study on cellular networks was performed, assuming no inter-cell interference and small-scale fading effect. Work in [26] examined the coverage and rate performance of mm-wave cellular networks, through a stochastic geometry framework. Different parameters of Nakagami fading were assumed for line-of-sight (LOS) and non-line-of-sight (NLOS) links, as well as directional antennas. A LOS ball-based blockage model was adopted, in which all nearby base stations were assumed LOS and all the other base stations over a certain distance were ignored.

Joint study of RIS with non-orthogonal multiple access (NOMA) has been recently an attractive research topic [27]–[30]. There exist two dominant NOMA schemes: the first is relevant to power domain multiplexing, which assumes that different users are allocated different transmission power, based on their channel conditions; the second is relevant to code domain multiplexing, which assumes that different users are assigned different codes, multiplexed over the same time-frequency resources. Complexity of successive interference cancellation (SIC) in both schemes was studied.

Work in [31]–[35] proposed metasurfaces in order to manipulate electromagnetic (EM) waves, allowing for anomalous reflection, full EM absorption, refraction, and polarization control. In [31], [34], [35] an application programming interface (API) is envisioned to exist on a server, in order to control the metasurfaces. Evaluations, solely based on simulations, showed improved received power and coverage.

A small number of experimental testbeds has recently emerged, e.g., work in [36]–[39]; [36] offered a 36-element array, with phase shifters helping endpoints whose line-of-sight (LoS) is blocked; [37] developed a RIS with 256 elements exploiting positive intrinsic-negative (PIN) diodes for 2−bit phase shifting; [38] utilized software-controlled, 2-load RF switches in groups, in order to select different surface configurations with thousands of elements, exploiting feedback from the destination; a RIS-based system was implemented in [39] with 256 elements (controlled with varactor diodes), which could facilitate amplitude-and-phase-varying modulation, assisting 2×2 MIMO transmission. In principle, each element should be controlled by a dedicated digital-to-analog converter (DAC). Due to hardware limitations however, two DACs were used in order to control the elements. The distance between the RIS and the two receiving antennas was about 1.5 meters and cables were required to control the RIS elements from a dedicated field programmable gate array (FPGA). All offered testbeds so far are based on wired prototypes.

B. Contribution

This work exploits commodity, ultra-low cost, commercial radio frequency identification tags *as the RIS elements*. Such batteryless tags are powered and controlled by a software-defined radio (SDR) reader, operating at carrier frequency f_2, with properly modified software, so that a source-destination link, operating at a *different* carrier frequency f_1, is assisted (Fig. 1).

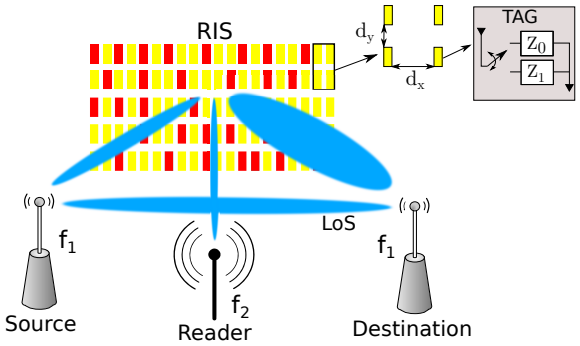

Fig. 1: The proposed wireless surface with commodity, wirelessly-controlled, RF-powered, RFID tags.

It is found for the first time in the literature (to the best of our knowledge): a) the optimal gain and corresponding best RIS element configuration, with tractable polynomial complexity (instead of exponential) in number of elements and b) the way to design and prototype a wireless, batteryless, RF-powered RIS, with commodity RFID tags. Future extensions at various carrier frequencies could be accommodated, through simple modifications in the antenna and matching network of each RFID tag, as well as modifications in the RFID protocol for efficient, RIS-tailored operation. The contributions are summarized as follows:

- Signal model includes small-scale and large-scale fading, as well as specific parameters relevant to reflection (i.e., backscatter) radio, such as antenna structural mode and reflection efficiency, typically overlooked in the literature; such modeling is critical in RIS-relevant research, due to the lack of amplification, the passive nature of reflecting elements and thus, the inherently weak signals involved.
- An algorithm that computes the optimal RIS configuration with tractable polynomial complexity of $O(M \log M)$, instead of intractable complexity of K^M for exhaustive search with large M, where $K \geq 2$ is the number of loads per RIS element and M is the total number of RIS elements. The algorithm can accommodate *any* set of reflection coefficients (e.g., not necessarily of common amplitude). Such algorithm allows for careful communication theory studies when M is in the order of thousands.
- It is numerically demonstrated that performance gain will reach a plateau if RIS element spacing is kept constant, for increasing number of elements in the order of thousands, using the proposed optimization method. This finding corroborates recent reports on bounded RIS performance and suggests that even with perfect channel estimation, the weak nature of backscattered links limits the performance gains, even for large number of RIS elements. Numerical results also suggest that amplification may be needed in practical setups.
- Issues relevant to CSI estimation are studied, including the linear minimum mean squared error (LMMSE) estimator and its performance, especially with large M at the

RIS.

- A RIS prototype is demonstrated, which is completely wireless and batteryless, using commercial (Gen2) RFID tags as the RIS elements. The surface is controlled by a software-defined radio reader, running a carefully modified stack of the Gen2 RFID protocol. Experimental results offer, to the best of our knowledge, the first wireless, batteryless RIS and future modifications and enhancements are also proposed.

C. Organization

The rest of the work is organized as follows. Section II offers a detailed system and signal model, tailored to the weak nature of backscattered signals; Section III offers the algorithm that can compute the optimal RIS configuration, given CSI, with tractable complexity; Section IV studies CSI estimation in RIS with large number of elements and LMMSE estimator; Section V describes the batteryless, wireless RIS implementation; Section VI offers evaluation, both in terms of simulations, as well as experimental results. Finally, work is concluded in Section VII.

Notation: $\mathbf{0}_N$ denotes the all-zeros vector. The phase of complex number z is denoted as $\angle z$, while $\Re\{z\}$ denotes the real part of z. The distribution of a proper complex Gaussian $N \times 1$ vector $\boldsymbol{x}$ with mean $\boldsymbol{\mu}$ and covariance matrix $\boldsymbol{\Sigma}$ is denoted by $\mathcal{CN}(\boldsymbol{\mu}, \boldsymbol{\Sigma}) \triangleq \frac{1}{\pi^N \det(\Sigma)} \mathrm{e}^{-(\boldsymbol{x}-\boldsymbol{\mu})^H \boldsymbol{\Sigma}^{-1}(\boldsymbol{x}-\boldsymbol{\mu})}$; the special case of a circularly symmetric complex Gaussian $N \times 1$ vector corresponds by definition to $\mathcal{CN}(\mathbf{0}_N, \boldsymbol{\Sigma})$; expectation of function $\mathrm{g}(\cdot)$ of random variable x is denoted by $\mathbb{E}[\mathrm{g}(x)]$.

II. System Model

A. Channel Model

A source-destination link is assisted by an array of M tags/RIS elements. The following *large-scale* channel path-loss model is adopted [40]:

$$\mathsf{L}_{\mathrm{X}} \propto \left(\frac{\lambda}{4\pi d_0^{\mathrm{X}}}\right)^2 \left(\frac{d_0^{\mathrm{X}}}{d_{\mathrm{X}}}\right)^{v_{\mathrm{X}}}, \tag{1}$$

where $\mathrm{X} \in \{\mathrm{SD}, \mathrm{ST}_m, \mathrm{T}_m\mathrm{D}\}$ denotes the source-to-destination, source-to-tag m and tag m-to-destination, respectively; λ is the carrier wavelength, d_0^{X} is a reference distance, v_{X} is the path-loss exponent and d_{X} is the distance for link X.

Flat fading is assumed; complex channel coefficients h_{SD}, h_{ST_m} and $h_{\mathrm{T}_m\mathrm{D}}$ denote the baseband channel coefficients for the source-destination, source-tag and tag-reader link, respectively. Due to strong line-of-sight (LoS) signals present in the problem, *small-scale* Rice flat fading channel model [40] is mainly adopted:[1]

$$h_{\mathrm{T}_m\mathrm{D}} \sim \mathcal{CN}\left(\sqrt{\frac{\kappa_{\mathrm{T}_m\mathrm{D}}}{\kappa_{\mathrm{T}_m\mathrm{D}}+1}}\,\sigma_{\mathrm{T}_m\mathrm{D}}, \frac{\sigma^2_{\mathrm{T}_m\mathrm{D}}}{\kappa_{\mathrm{T}_m\mathrm{D}}+1}\right), \tag{2}$$

[1]The complex channel is the superposition of $\sqrt{\frac{\kappa_{\mathrm{T}_m\mathrm{D}}}{\kappa_{\mathrm{T}_m\mathrm{D}}+1}}\,\sigma_{\mathrm{T}_m\mathrm{D}}\, e^{j\theta}$ + $\mathcal{CN}\left(0, \frac{\sigma^2_{\mathrm{T}_m\mathrm{D}}}{\kappa_{\mathrm{T}_m\mathrm{D}}+1}\right)$ with random θ.

where $h_{\mathrm{T}_m\mathrm{D}} \triangleq |h_{\mathrm{T}_m\mathrm{D}}|\, e^{-j\phi_{\mathrm{T}_m\mathrm{D}}}$, $k_{\mathrm{T}_m\mathrm{D}}$ is the power ratio between the deterministic LoS component and the scattering components and $\mathbb{E}[|h_{\mathrm{T}_m\mathrm{D}}|^2] = \sigma^2_{h_{\mathrm{T}_m\mathrm{D}}}$ is the average power of the scattering components. For link budget normalization purposes, $\sigma^2_{h_{\mathrm{T}_m\mathrm{D}}} = 1$ will be also assumed (other values could be easily accommodated into the large-scale, average coefficients). Similar notation and assumptions hold for h_{ST_m}, $m \in \{1, 2, \ldots, M\}$ and h_{SD}. It is noted that for $\kappa = 0$, Rice is simplified to Rayleigh fading.

Quasi-static block fading is assumed, i.e., the channel remains constant for L_c (source-destination link) symbols and changes independently between channel coherence time periods. Channel coefficients h_{SD}, $\{h_{\mathrm{ST}_m}\}$, $\{h_{\mathrm{T}_m\mathrm{D}}\}$, $m \in \{1, 2, \ldots, M\}$ are assumed independent in the numerical results. Furthermore, the following notation is also adopted:

$$\begin{aligned} h_m &= h_{\mathrm{ST}_m}\, h_{\mathrm{T}_m\mathrm{D}} = |h_{\mathrm{ST}_m}\, h_{\mathrm{T}_m\mathrm{D}}|\, e^{-j\phi_m}, m \in \{1, 2, \ldots, M\}, \\ h_0 &= h_{\mathrm{SD}}, m = 0. \end{aligned} \tag{3}$$

B. Signal Model

The baseband source message $c(t)$ is given by:

$$c(t) = \sqrt{2P}\, m(t) \tag{4}$$

where $\mathbb{E}[|m(t)|^2] = 1$. Different normalization could be incorporated into the large-scale coefficients. The baseband complex equivalent of the scattered waveform from tag m follows [5]:

$$u_m(t) = \sqrt{\eta\, \mathsf{L}_{\mathrm{ST}_m}}\, [A_s - \Gamma_m(t)]\, h_{\mathrm{ST}_m}\, c(t), \tag{5}$$

$$\Gamma_m(t) \in \{\Gamma_1, \Gamma_2, \ldots, \Gamma_K\}, \tag{6}$$

where $\Gamma_m(t)$ stands for the modified (complex) reflection coefficient for tag m, assuming that the tag can terminate its antenna between K loads and η models the (limited) tag power scattering efficiency. It is noted that for passive (amplification-free) tags, $|\Gamma_k| \leq 1$, while for commercial RFID tags, $K = 2$. Parameter A_s stands for the load-independent *structural mode* that solely depends on tag's antenna [41], commonly overlooked in the literature; $A_s = 1$ only for *minimum scattering* antennas, i.e., antennas that do not reflect anything when terminated at open (i.e., infinite) load, corresponding to unit reflection coefficient (and in that case $A_s - \Gamma = 0$).

The received demodulated complex baseband signal at the destination is given by the superposition of the source and all tags' backscattered signals propagated through wireless channels h_{SD} and $\{h_{\mathrm{T}_m\mathrm{D}}\}$, respectively:

$$\begin{aligned} y(t) &= \sqrt{\mathsf{L}_{\mathrm{SD}}}\, h_{\mathrm{SD}}\, c(t) + \sum_{m=1}^{M} \sqrt{\mathsf{L}_{\mathrm{T}_m\mathrm{D}}}\, h_{\mathrm{T}_m\mathrm{D}}\, u_m(t) + n(t) \\ &= \sqrt{\mathsf{L}_{\mathrm{SD}}}\, h_{\mathrm{SD}}\, c(t) + n(t) \\ &\quad + \sum_{m=1}^{M} \sqrt{\eta\, \mathsf{L}_{\mathrm{ST}_m} \mathsf{L}_{\mathrm{T}_m\mathrm{D}}}\, h_{\mathrm{ST}_m}\, h_{\mathrm{T}_m\mathrm{D}}\, [A_s - \Gamma_m(t)]\, c(t) \\ &= \sqrt{2P} \left[\sqrt{g_0}\, h_0 + \sum_{m=1}^{M} \sqrt{g_m}\, h_m\, \mathcal{Y}_m(t)\right] m(t) + n(t), \end{aligned} \tag{7}$$

where $n(t)$ is the thermal noise at the receiver and

$$g_0 = \mathsf{L}_{\mathrm{SD}}, \tag{8}$$

$$g_m = \eta\, \mathsf{L}_{\mathrm{ST}_m} \mathsf{L}_{\mathrm{T}_m\mathrm{D}}\, \mathbb{E}\left[|A_s - \Gamma_m(t)|^2\right], \tag{9}$$

$$\mathcal{Y}_m(t) = \frac{A_s - \Gamma_m(t)}{\sqrt{\mathbb{E}\left[|A_s - \Gamma_m(t)|^2\right]}}, \tag{10}$$

$$y_m\left[\Gamma_m(t)\right] \triangleq \sqrt{g_m}\, h_m\, \mathcal{Y}_m(t). \tag{11}$$

Notice that $\mathbb{E}[|h_0|^2] = \mathbb{E}[|h_m|^2] = \mathbb{E}[|\mathcal{Y}_m|^2] = 1$ since $\mathbb{E}[|h_m|^2] = \mathbb{E}[|h_{\mathrm{ST}_m}|^2]\,\mathbb{E}[|h_{\mathrm{T}_m\mathrm{D}}|^2]$, due to the followed assumptions. It is also noted that $\mathbb{E}\left[|A_s - \Gamma_m(t)|^2\right] = (1/K)\sum_{k=1}^{K} |A_s - \Gamma_k|^2$.

The above model is valid when coupling among the tags is negligible, i.e., the tags are separated by distance at least equal to $\lambda/2$. Additive thermal noise $n(t)$ is modelled by a complex, circularly symmetric, additive Gaussian noise process with $\mathbb{E}[|n(t)|^2] = N_0 B$, where B stands for receiver's bandwidth.[2]

III. Optimal Configuration for Maximum Gain

RIS targets at SNR improvement, by controlling the environment, through proper selection of the reflection coefficient at each element. According to Eq. (7), the following instantaneous power maximization problem is formulated:

$$\max_{\{\mathcal{Y}_m(t)\}} \left|\sqrt{g_0}\, h_0 + \sum_{m=1}^{M} \sqrt{g_m}\, h_m\, \mathcal{Y}_m(t)\right|^2 2P \tag{12}$$

$$\Leftrightarrow \max_{\{\mathcal{Y}_m(t)\}} \left|\underbrace{\sqrt{g_0}\, h_0}_{y_0} + \sum_{m=1}^{M} \sqrt{g_m}\, h_m\, \mathcal{Y}_m(t)\right| \tag{13}$$

$$= \max_{\{\Gamma_m(t)\}} \left|y_0 + \sum_{m=1}^{M} y_m\left[\Gamma_{m(t)}\right]\right|, \tag{14}$$

which cannot be solved with exhaustive search, since each RIS element (among M elements) can select among K loads, i.e., $\Gamma_m(t) \in \{\Gamma_1, \Gamma_2, \ldots, \Gamma_K\}$, and thus, there are K^M possible load configurations. Even for $K = 2$ and $M = 100$, exhaustive search among 2^{100} load configurations is not an option.

The following offers an *optimal* method for the above optimization problem, with log-linear complexity $O(M \log(M))$ in the number M of RIS elements, instead of the exponential (in M) complexity of exhaustive search.

The problem above is similar to noncoherent sequence detection of orthogonally-modulated sequences, solved with polynomial complexity in [42]. The trick is to introduce an auxiliary scalar variable ϕ into the problem of Eq. (14):

$$\max_{\{\Gamma_m(t)\}} \max_{\phi\in[0,2\pi)} \Re\left\{e^{-j\phi}\left(y_0 + \sum_{m=1}^{M} y_m\left[\Gamma_{m(t)}\right]\right)\right\} =$$

$$\max_{\phi\in[0,2\pi)} \max_{\{\Gamma_m(t)\}} \left(\Re\left\{e^{-j\phi} y_0\right\} + \sum_{m=1}^{M} \Re\left\{e^{-j\phi} y_m\left[\Gamma_{m(t)}\right]\right\}\right) \tag{15}$$

[2] $N_0 = k_b T_\theta$, where k_b and T_θ are the Boltzmann constant and receiver temperature, respectively.

A. $K = 2$ Loads

For a given point $\phi \in [0, 2\pi)$, the innermost maximization in Eq. (15) is separable for each $\Gamma_m(t)$ and hence, splits into independent maximizations for any $m = 1, 2, \ldots, M$:

$$\begin{aligned}
\hat{\Gamma}_m(t) &= \underset{\Gamma_m(t)\in\{\Gamma_1,\Gamma_2\}}{\arg\max}\ \Re\left\{\mathrm{e}^{-j\phi} y_m\left[\Gamma_m(t)\right]\right\} \\
&\Leftrightarrow \Re\left\{\mathrm{e}^{-j\phi} y_m\left[\Gamma_1\right]\right\} \underset{\hat{\Gamma}_m(t)=\Gamma_2}{\overset{\hat{\Gamma}_m(t)=\Gamma_1}{\gtrless}} \Re\left\{\mathrm{e}^{-j\phi} y_m\left[\Gamma_2\right]\right\} \\
&\Leftrightarrow \Re\left\{\mathrm{e}^{-j\phi}\left(y_m\left[\Gamma_1\right] - y_m\left[\Gamma_2\right]\right)\right\} \underset{\hat{\Gamma}_m(t)=\Gamma_2}{\overset{\hat{\Gamma}_m(t)=\Gamma_1}{\gtrless}} 0 \\
&\Leftrightarrow \cos\left(\phi - \angle\underline{y_m\left[\Gamma_1\right] - y_m\left[\Gamma_2\right]}\right) \underset{\hat{\Gamma}_m(t)=\Gamma_2}{\overset{\hat{\Gamma}_m(t)=\Gamma_1}{\gtrless}} 0
\end{aligned} \tag{16}$$

Given the relation in Eq. (15), the optimal load sequence $\hat{\mathbf{\Gamma}}^{\mathrm{opt}}$ can be found by varying ϕ from 0 to 2π. It is further noticed that, as ϕ scans $[0, 2\pi)$, the decision $\hat{\Gamma}_m(t)$ changes, according to Eq. (16), only when:

$$\begin{aligned}
&\cos\left(\phi - \angle\underline{y_m\left[\Gamma_1\right] - y_m\left[\Gamma_2\right]}\right) = 0 \\
&\Leftrightarrow \phi = \underbrace{\pm\frac{\pi}{2} + \angle\underline{y_m\left[\Gamma_1\right] - y_m\left[\Gamma_2\right]} \pmod{2\pi}}_{\phi_m^{(1)},\phi_m^{(2)}}.
\end{aligned}$$

Therefore, the sequence $\hat{\mathbf{\Gamma}} = \left[\hat{\Gamma}_1(t), \hat{\Gamma}_2(t), \ldots, \hat{\Gamma}_M(t)\right]^T$ changes only at

$$\left(\phi_1^{(1)}, \phi_1^{(2)}, \phi_2^{(1)}, \phi_2^{(2)}, \cdots, \phi_M^{(1)}, \phi_M^{(2)}\right).$$

For the remaining part of this section, we assume that the above $2M$ points are distinct and nonzero, i.e., $\phi_m^{(j)} \neq \phi_l^{(k)}$ and $\phi_m^{(j)} \neq 0$, for any $j, k, \in \{1, 2\}$ and $m, l \in \{1, 2, \ldots, M\}$ with $m \neq l$. There is a case where the above assumption does not hold, examined in [42]. If the above points are sorted in ascending order, i.e.,

$$(\theta_1, \theta_2, \cdots, \theta_{2M}) = \mathsf{sort}\left(\phi_1^{(1)}, \phi_1^{(2)}, \phi_2^{(1)}, \phi_2^{(2)}, \cdots, \phi_M^{(1)}, \phi_M^{(2)}\right), \tag{17}$$

then the decision $\hat{\mathbf{\Gamma}}$ will remain constant in each one of the $2M + 1$ intervals $(\theta_i, \theta_{i+1}), i \in \{0, 1, \ldots, 2M\}$, with $\theta_0 = 0$ and $\theta_{2M+1} = 2\pi$. The goal is the identification of the $2M + 1$ sequences that correspond to these intervals,[3] one of which gives the optimal $\hat{\mathbf{\Gamma}}^{\mathrm{opt}}$, i.e., the one that offers the maximum power; thus, the quality of each sequence is calculated with the norm metric of Eq. (14), which explicitly includes the direct channel h_0. Based on the above, the sorting operation in Eq. (17) is dominant in terms of computational cost, which is $O(M \log M)$ and not 2^M.

B. $K > 2$ Loads

The method described above can be generalized to $K > 2$ loads, i.e., $\Gamma_m(t)$ belongs in $\{\Gamma_1, \Gamma_2, \ldots, \Gamma_K\}$. The solution is given by selecting the largest value of $\Re\left\{\mathrm{e}^{-j\phi} y_m[\Gamma_k]\right\}$ among all $k \in \{1, 2, \ldots K\}$, which results in testing $2M \times (K - 1)$

[3] It can be shown that the sequence at $[0, \theta_1)$ is the same with the sequence at $[\theta_{2M}, 2\pi)$ and thus, $2M$ intervals/sequences should be identified.

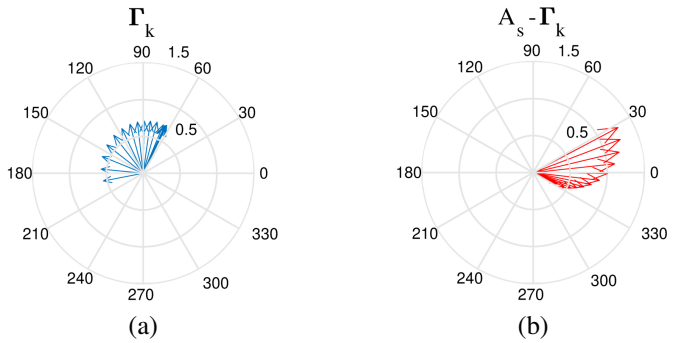

Fig. 2: The 21 reflection coefficients used in the simulations.

changes of ϕ and as a result, same number of sequence changes and not $2M \times \binom{K}{2}$, as one would expect; the rest of the steps are exactly the same as in $K = 2$. Formal proof and details can be found in [42]. Notice that the norm metric for the quality of each sequence must include h_0. The complexity of the algorithm is not K^M, but again $O(M \log M)$ for $M > K$.[4]

Fig. 2(a) depicts $K = 21$ (complex) reflection coefficients, corresponding to the 21 loads, offered through a varactor at each tag, as experimentally tested in [44]. It can be shown that these reflection coefficients span more than 120°. Fig. 2(b) shows $A_s - \Gamma_k, k \in \{1, 2, \dots K\}$, which incorporates the contribution of the structural mode of each RIS element antenna, typically overlooked in the literature; it can be seen that the span of $A_s - \Gamma_k$ in degrees is much smaller, in the order of 60°.

IV. Channel Estimation Overhead

It is assumed that the channel coherence time spans L symbols and $\alpha \times L$ is the number of symbols devoted for pilot transmission, necessary for channel estimation, i.e., α is the percentage of channel coherence time devoted for channel estimation. The following expressions hold for Rayleigh and Rice fading, for a RIS with M elements plus the direct link ($m \in \{0, 1, 2, \dots M\}$).

To estimate the $(M+1)$ channel coefficients, the linear minimum mean squared error (LMMSE) estimator was applied. The aforementioned estimator is an affine transformation of the sampled received signal $y(t)$, i.e. $\hat{h}_m = \mathbf{a}_m^{\mathrm{H}} \mathbf{y} + b_m$, where $\mathbf{a}_m, \mathbf{y} \in \mathbb{C}^{N_{\mathrm{tr}} \times 1}$, $b_m \in \mathbb{C}$ and $N_{\mathrm{tr}} = \frac{\alpha L}{M+1}$ are the training symbols devoted to the estimation of each h_m.[5] Parameters $\mathbf{a}_m$ and b_m can be computed in closed form as follows [45], [46], [47]:

$$\mathbf{a}_m = C_{\mathbf{y}}^{-1} C_{\mathbf{y}h_m}, \tag{18}$$

and

$$b_m = \mu_{h_m} - \mathbf{a}_m^{\mathrm{H}} \mu_{\mathbf{y}}, \tag{19}$$

where $\mu_{\mathbf{y}} \triangleq \mathbb{E}[\mathbf{y}]$, $C_{\mathbf{y}} \triangleq \mathbb{E}[(\mathbf{y} - \mu_{\mathbf{y}})(\mathbf{y} - \mu_{\mathbf{y}})^{\mathrm{H}}]$ is the covariance matrix of $\mathbf{y}$, $\mu_{h_m} \triangleq \mathbb{E}[h_m]$ and $C_{\mathbf{y}h_m} \triangleq \mathbb{E}[(\mathbf{y} - \mu_{\mathbf{y}})(h_m - \mu_{h_m})^*]$ is the cross-covariance vector between $\mathbf{y}$ and h_m. The mean squared estimation error of this linear estimator is given by [45], [46], [47]:

$$\mathsf{MSE} = \sigma_{h_m}^2 - C_{h_m \mathbf{y}} C_{\mathbf{y}}^{-1} C_{\mathbf{y}h_m}, \tag{20}$$

where $\sigma_{h_m}^2 \triangleq \mathbb{E}\left[(h_m - \mathbb{E}[h_m])(h_m - \mathbb{E}[h_m])^*\right] \equiv \mathbb{E}\left[|h_m - \mathbb{E}[h_m]|^2\right] = \mathbb{E}[|h_m|^2] - |\mathbb{E}[h_m]|^2$ and $C_{h_m \mathbf{y}} = C_{\mathbf{y}h_m}^{\mathrm{H}}$.

It is further assumed that for any $K \geq 2$ loads per RIS element, there exist two loads that correspond to reflection coefficient $\Gamma_m(t) = 0$ and $\Gamma_m(t) = A_s$. In order to estimate all RIS coefficients, estimation of h_0 is a preceding necessity. If all tags are terminated to a load such that $\Gamma_m(t) = A_s$ for all RIS elements ($m \in \{1, 2, \dots, M\}$), then during channel estimation phase for the direct link and (respective) pilot symbols transmission from the source, Eq. (7) will be simplified as follows:

$$\mathbf{y}_0 = \sqrt{2Pg_0}\, h_0\, \mathbf{m} + \mathbf{n}, \tag{21}$$

where $\mathbf{m}, \mathbf{n} \in \mathbb{C}^{N_{\mathrm{tr}} \times 1}$, $\mathbf{n}$ is a circularly symmetric complex Gaussian vector with independent elements and $\mathbf{m}$ is the vector of the pilot symbols, which satisfies $\mathbf{m}^{\mathrm{H}} \mathbf{m} = N_{\mathrm{tr}}$ [48]. After normalizing with the noise power, Eq. (21) becomes as follows:

$$\bar{\mathbf{y}}_0 = \sqrt{\mathsf{SNR}_0}\, h_0\, \mathbf{m} + \bar{\mathbf{n}}, \tag{22}$$

where $\bar{\mathbf{n}} \sim \mathcal{CN}(\mathbf{0}, \mathbf{I}_{N_{\mathrm{tr}}})$ and $\mathsf{SNR}_0 \triangleq \frac{2Pg_0}{N_0 B}$, from which one can calculate the covariance matrices and derive the optimal $\mathbf{a}_0$ and b_0. The specific formulas will be given below.[6]

After estimation of h_0 is completed, the estimation of h_m follows, for a specific $m \neq 0$: for N_{tr} training symbols, the m-th RIS element of interest is terminated at a load such that $\Gamma_m(t) = 0$ and all the rest RIS elements are terminated to load such that $\Gamma_{m'}(t) = A_s$, $m' \neq m$, $\forall\, m' \in \{1, 2, \dots, M\}$. The same procedure is repeated for all RIS elements. Assuming h_0 is optimally estimated, the following relation concerning the m-th tag follows, stemming directly from Eq. (7) with the choice of the above reflection coefficients:

$$\mathbf{y}_m \triangleq \mathbf{y} - \sqrt{2Pg_0}\, \hat{h}_0\, \mathbf{m} = \sqrt{2Pg_m}\, \mathcal{Y}_m\, (\Gamma_m = 0)\; h_m\, \mathbf{m} + \mathbf{n}, \tag{23}$$

with $m \in \{1, 2, \dots M\}$. Eq. (23) and Eq. (21) are almost identical; the only difference is the constant term $\mathcal{Y}_m\, (\Gamma_m = 0)$, which for $m = 0$ is equivalent to setting $\mathcal{Y}_0 = 1$. Normalizing with the noise power in Eq. (23) yields:

$$\bar{\mathbf{y}}_m = \sqrt{\mathsf{SNR}_m}\, \mathcal{Y}_m\, (\Gamma_m = 0)\; h_m\, \mathbf{m} + \bar{\mathbf{n}}, \tag{24}$$

where $\bar{\mathbf{n}} \sim \mathcal{CN}(\mathbf{0}, \mathbf{I}_{N_{\mathrm{tr}}})$ and $\mathsf{SNR}_m = \frac{2Pg_m}{N_0 B}$, $m \in \{1, \dots, M\}$. The following lemma offers the estimation results:

Lemma 1. *For both Rayleigh and Rice fading, $m \in \{0, 1, 2, \dots M\}$, the minimum MSE linear estimator and cor-*

[4] During review and revision of this work, one of the reviewers pointed towards [43], which however offers suboptimal gain for $K > 2$ loads per element; for $K = 2$ loads, the algorithm there requires sorting of $2M + 2$ phases [43, page 970, first column, definition of $2M + 2$ arcs in $[0, 2\pi)$], and thus obtains complexity of $O(M \log(M))$.

[5] α is selected in such way so that N_{tr} is a positive integer.

[6] It is assumed that the constant, deterministic terms, such as g_m or SNR_m have been already estimated; this is practically possible for immobile scenarios or scenarios with extended channel coherence time. In such cases, it can be numerically shown that constants can be estimated in a straightforward manner.

responding MSE, for the procedure described above, is given by:

$$\hat{h}_m = \frac{\sigma_{h_m}^2 \sqrt{SNR_m}\, \mathcal{Y}_m^* (\Gamma_m = 0)\ \mathbf{m}^{\mathrm{H}} \mathbf{y} + \mu_{h_m}}{1 + N_{tr}\, \sigma_{h_m}^2\, |\mathcal{Y}_m (\Gamma_m = 0)|^2\, SNR_m}, \tag{25}$$

$$MSE_m = \frac{\sigma_{h_m}^2}{1 + N_{tr}\, \sigma_{h_m}^2\, |\mathcal{Y}_m (\Gamma_m = 0)|^2\, SNR_m}, \tag{26}$$

where $\mathbb{E}[|h_m|^2] = 1, \forall m \in \{0, 1, \ldots, M\}$ *and* $\mathcal{Y}_0 = 1$ *for both fading cases, while* $\mathbb{E}[h_m] \triangleq \mu_{h_m} = 0$, $\sigma_{h_m}^2 = 1, \forall m \in \{0, 1, \ldots, M\}$ *for Rayleigh fading and* $\mathbb{E}[h_m] = \mu_{h_m} \neq 0$, $\sigma_{h_m}^2 \triangleq \mathbb{E}[|h_m|^2] - |\mathbb{E}[h_m]|^2 = 1 - |\mu_{h_m}|^2, \forall m \in \{0, 1, \ldots, M\}$ *for Rice fading.*

Proof. Based on Eqs. (22), (24) and having in mind that $\mathcal{Y}_0 = 1$, the necessary parameters in Eqs. (18), (19), (20) are computed as follows:

$$C_{\mathbf{y}h_m} = \sigma_{h_m}^2 \sqrt{\mathrm{SNR}_m}\, \mathcal{Y}_m\, \mathbf{m},$$

$$C_{\mathbf{y}} = \sigma_{h_m}^2\, |\mathcal{Y}_m (\Gamma_m = 0)|^2\, \mathrm{SNR}_m\, \mathbf{m}\, \mathbf{m}^{\mathrm{H}} + \mathbf{I}_{N_{\mathrm{tr}}}.$$

Substituting in Eqs. (18), (19), (20) and exploiting the *push-through* matrix identity, offers the above expressions. ∎

The lemma requires $\mathcal{Y}_m(t)$, for $m \neq 0$. This is simply given by the following formulas:

A. K=2

$$\mathcal{Y}_m(t) = \frac{A_s - \Gamma_m(t)}{\sqrt{\mathbb{E}\left[|A_s - \Gamma_m(t)|^2\right]}} = \begin{cases} \dfrac{A_s - 0}{\sqrt{\frac{|A_s - 0|^2 + |A_s - A_s|^2}{1+1}}}, \Gamma_m = 0 \\ \dfrac{A_s - A_s}{\sqrt{\frac{|A_s - 0|^2 + |A_s - A_s|^2}{1+1}}}, \Gamma_m = A_s \end{cases}$$

$$= \begin{cases} \sqrt{2}\, \dfrac{A_s}{|A_s|}, \Gamma_m = 0 \\ 0, \ \Gamma_m = A_s. \end{cases}$$

B. K > 2 Loads

$$\mathcal{Y}_m(t) = \frac{A_s - \Gamma_m(t)}{\sqrt{\mathbb{E}\left[|A_s - \Gamma_m(t)|^2\right]}}$$

$$= \begin{cases} \dfrac{A_s - \Gamma_k}{\sqrt{(1/K) \sum_{k=1}^{K} |A_s - \Gamma_k|^2}}, \ \Gamma_m = \Gamma_k \\ \dfrac{A_s - A_s}{\sqrt{(1/K) \sum_{k=1}^{K} |A_s - \Gamma_k|^2}}, \ \Gamma_m = A_s \end{cases}$$

$$= \begin{cases} \dfrac{\sqrt{K}\, (A_s - \Gamma_k)}{\sqrt{\sum_{k=1}^{K} |A_s - \Gamma_k|^2}}, \ \Gamma_m = \Gamma_k \\ 0 \qquad\qquad\qquad\quad , \ \Gamma_m = A_s \end{cases}$$

V. Wireless Batteryless Implementation

The RFID-based RIS is controlled by the RFID reader at carrier frequency f_2, through commands such as Select, Query and ACK, explained below. In the commercial RFID standard (EPC Gen2), a framed slotted Aloha (FSA) protocol is used, so that tags backscatter one at a time, without collision. For RIS purposes, the opposite is needed, i.e., tags must be forced to backscatter in carefully selected groups.

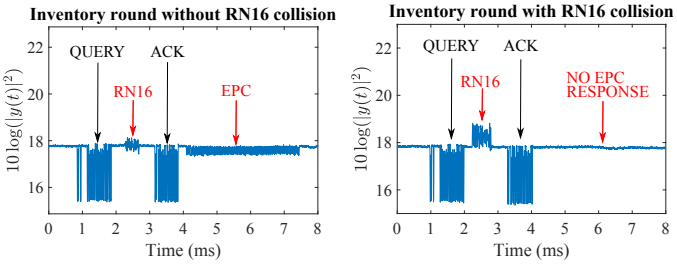

(a) No RN16 collision. (b) RN16 collision.

Fig. 3: Conventional Gen2 RFID operation from experimental measurements: each tag responds to a Query command with a random RN16 message; if it is correctly acknowledged, it will respond with its EPC.

In Gen2, the reader initiates the start of a frame with a Query command, which contains the number of slots. Ideally, the number of slots should be equal to the number of tags to be inventoried. If the reader advertises number of slots equal to 1, then all tags in the vicinity of the reader will respond. That was the approach followed in this work. Then, each tag responds with a random 16-bit number, namely the RN16 message, which is in principle different among the competing tags. If the reader correctly decodes that message then it will send the ACK command, containing the RN16 sent by the tag. Collision detection and error detection is conducted at the reader using the line coding the tags incorporate (FM0 or Miller).[7] If the tag is correctly acknowledged, it will reply with its ID (EPC); the latter is typically 96−bits payload plus CRC bits. Fig. 3(a) depicts an inventory round with an acknowledged tag, while in Fig. 3(b) multiple tags have backscattered their RN16, resulting to a collision; this is the case exploited in this work.

The RN16 is preceded by a 6-bit Preamble sequence, which does not follow the line coding rules and is the same for all tags. As a result, using the Preamble one could measure the effect of a specific RIS *configuration* (where configuration denotes the set of tags that change their reflection coefficients, among the total number of RIS tags). Since the random 16-bit sequence of the RN16 is different for each tag, the signal level (or the effective channel) during RN16 could be higher or lower than the Preamble level because only a subset of the configuration's tags are terminated at the same load at a given point of time. This is shown in Fig. 4.

In the Gen2 industrial RFID standard, the Select command (issued by the Reader) is asserting or deasserting the SL flag of the tags. When a tag has its SL flag asserted, it responds

[7]The reader directs the tags about the line code they are going to use.

with an RN16 after a Query command. The Select command contains a mask with a specified length and starting point. Each tag compares this mask with its corresponding EPC bits. The Action parameter, which is a field set by the reader during the Select command, allows the user to specify how the SL flag will change if the mask matches the EPC of the tag. To assert a specific tag's SL flag without affecting the others', the Action parameter is set to $\{0, 0, 1\}$. To deassert all SL flags with one Select, the Action parameter is set to $\{0, 0, 0\}$ and the mask is set to avoid corresponding to any tag.

For RIS purposes, a *specific* configuration is set by having the reader issuing successive Select commands and asserting the SL flag of the specified tags, sequentially. This is shown in Fig. 5. First, a continuous wave (CW) energizes the tags and then the Select commands are issued. Afterwards, we can observe 10 inventory rounds (Query-RN16-ACK), where the peaks are the superposition of the RN16 from the selected tags. Finally, to advance to a new configuration, another Select is sent but with Action parameter equal to $\{0, 0, 0\}$ and a non-matching mask to any tag.

In Fig. 6 we observe a sequence of 9 different configurations. Each configuration spans 10 inventory (Query-RN16-ACK) rounds. Different configurations offer different effective channel and hence, different maximum signal power. Those peaks occur at the Preamble+RN16 tag response, as explained in Fig. 5. It is noted that the measurements were conducted in a static indoor environment, with channel coherence time spanning several hundreds of msec (and thus, different peaks are due to different tag configurations and not changes in the channel). The time between the end of the last RN16 from one configuration and the start of the first RN16 from the next is specified as t_c. More specifically, by varying the backscatter link frequency (BLF) parameter, t_c changes accordingly. The dependence of t_c in number of tags selected at each configuration, is better explained by the following

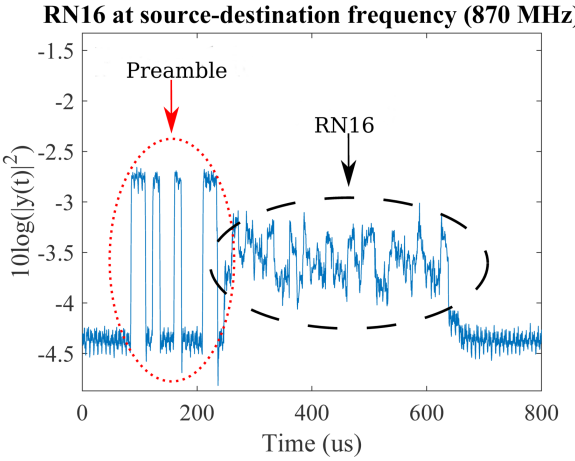

Fig. 4: Superposition of Preamble+RN16 from multiple tags.

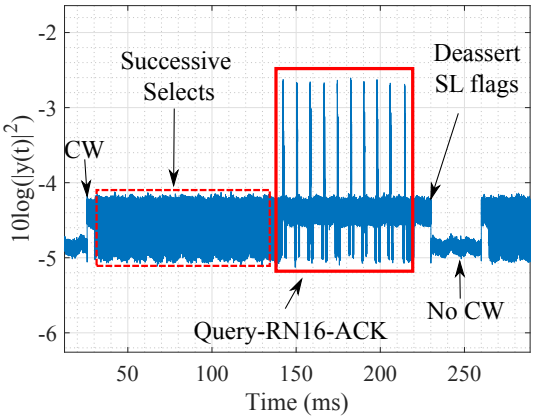

Fig. 5: Reader-Tag communication during a configuration.

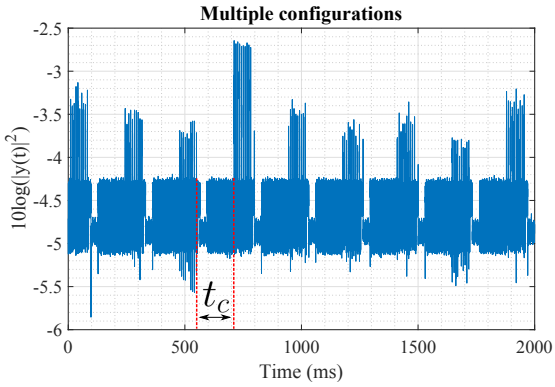

Fig. 6: Power at Destination during different configurations.

equation:

$$\begin{aligned} t_c &= (\mu+1)\,(\mathrm{T_{SELECT}} + \mathrm{T_4}) + \mathrm{T_{DELAY}} + \mathrm{T_{PU}} \\ &= (\mu+1)\left(61 \cdot \frac{1}{\mathrm{BLF}} \cdot 10^3 + 0.15\mathrm{ms}\right) \\ &\quad + 30\mathrm{ms} \;+ 184 \cdot \frac{1}{\mathrm{BLF}} \cdot 10^3 \end{aligned} \tag{27}$$

In Eq. (27), μ is the number of activated elements/tags in a configuration with μ Select commands asserting the SL flags and, at the end of the configuration, one deasserting them; $\mathrm{T_{SELECT}}$ is the duration of a Select and $\mathrm{T_4}$ is the minimum duration between successive reader commands; $\mathrm{T_{DELAY}}$ is a time interval at the end of the configuration where no commands or continuous wave (CW) is transmitted by the reader, shown in Fig. 5. This allows the tags to deassert their SL flags and was found heuristically for the specific RFID tags used, in the order of 30ms; backscatter-Link frequency $\mathrm{BLF} \in [40\ \mathrm{kHz}, 640\ \mathrm{kHz}]$ was set in the experimental setup equal to 40kHz. For time T_{PU}, the reader sends CW prior to the Select command to power-up the tags and set them to the Ready state. By varying the BLF parameter, t_c changes accordingly. For example, if $\mu = 50$, then $t_c \in [43\ \mathrm{ms}, 116\ \mathrm{ms}]$. In Fig. 6, $t_c = 116$ ms. Future RIS-friendly modifications of Gen2 could further reduce this parameter. For example, parameter $\mathrm{T_{DELAY}}$ should be decreased, the Select command should be

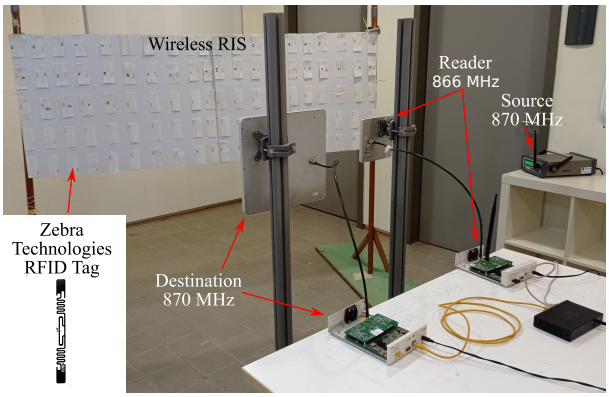

Fig. 7: Experimental setup.

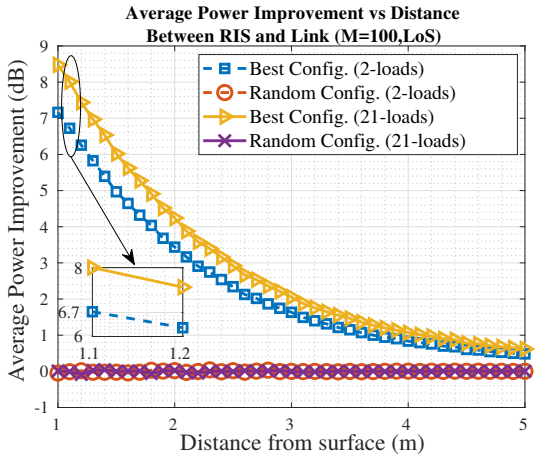

Fig. 8: Average Power Gain; tags' spacing $d_x = d_y = \frac{\lambda}{2}$.

reduced in size and parameter BLF should be increased as much as possible.

The experimental setup is depicted in Fig. 7, with M = 100 commodity Alien ALN-9840 Gen2 RFID tags, separated by d_x = 10 cm and d_y = 5 cm. The source-destination link operates at f_1 = 870 MHz, while the software-defined radio reader operates at f_2 = 866 MHz, with zero interference among the two channels. Modifications in the Gen2 reader software stack from [49] were conducted to enable RIS functionality. Two commodity USRP N200 software defined radios, each equipped with a RFX900 daughterboard, were utilized, both connected to a commodity laptop through a switch. One SDR was used as the Reader that controlled the RIS tags and the other was utilized as the destination. Source of the link was a signal generator at 870 MHz. The antennas used at the reader and source were circularly-polarized. It is emphasized that Figs. 3, 4, 5, 6 are offered from the SDR receiver at the destination.

Gen2 RFIDs are exploited as batteryless, wirelessly controlled reflective elements. Each RFID label requires an impinged RF power greater than its sensitivity threshold. In the case of the utilized ALN-9840 tags, an RFID reader should (typically) provide at least −17.8 dBm (−14.8 dBm if write operations are required) of RF power at the location of each tag [50].

VI. Numerical Results

A. Simulations

Figs. 8 and 9 are generated with typical indoor static conditions in mind: $\kappa_{\mathrm{ST}_m} = \kappa_{\mathrm{T}_m\mathrm{D}} = \kappa_{\mathrm{SD}} = \kappa = 8$, $v_{\mathrm{X}} = 3$; moreover, $\eta = 10\%$, $d_0^{\mathrm{X}} = d_{\mathrm{SD}} = 3$ m, $f_2 = 870$ MHz, $P = 5$ dBm, and 10 dB relative end-2-end antenna gain for the backscattered links compared to direct link, assuming that the source and destination antennas point towards the RIS, assisting its operation.

Fig. 8 offers the average power improvement due to RIS and direct link operation, compared to direct link communication only (without RIS). Several instances of the channels are generated, optimal configuration is found, for $K = 2$ or $K = 21$ loads per element and $M = 100$ RIS elements, based on the analysis of Section III and the average power improvement is reported. The SD link is parallel to RIS and

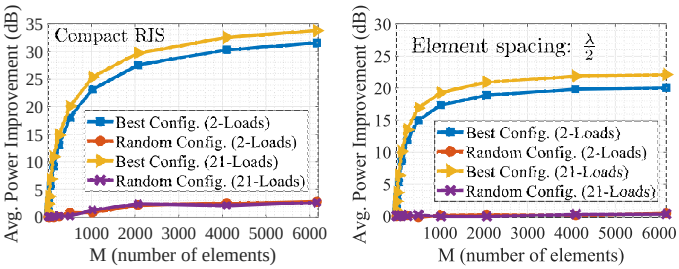

Fig. 9: Average power improvement (dB) vs number of RIS elements M.

distance from surface ($d_{\mathrm{RIS-SD}}$) is varied. It is noted that exhaustive search among $K^M = 2^{100}$ or 21^{100} configurations among RIS elements is practically impossible; however, results are offered based on the optimal gain discovery algorithm of Section III. It is observed that as the distance of the SD link from RIS increases, performance gains of optimal RIS operation decrease. That is due to the fact that backscattered links (through RIS) become weaker, as the distance of the SD link from the surface increases. This finding suggests that amplification at each RIS element (i.e., $|\Gamma_k| > 1$), i.e., *active* rather than passive RIS operation is needed; it is also important to carefully model the wireless channel, as well as the backscattering operation. Moreover, it is observed that using $K = 21$ loads for each element, despite the small angle span of the induced backscattered signals (explained in Sec. III-B), offers power gain in the order of 1.3 additional dB only, compared to $K = 2$. Perfect CSI is assumed in this figure, as well as in next Fig. 9 and Fig. 10; impact of CSI estimation is studied subsequently.

Fig. 9 offers average power improvement as a function of M, for two setups: Fig. 9(a) sets $d_x = 0.1$ m $< \lambda/2$ and $d_y = 0.05$ m $< \lambda/2$ (setup (a)), while Fig. 9(b) sets spacing between adjacent tags equal to $\lambda/2 = 0.172$ m (setup (b)). For both setups, $d_{\mathrm{SD}} = 3$ m, $d_{\mathrm{RIS-SD}} = 1$ m, while setup (a) ignores possible coupling between adjacent tags. It is found that performance in setup (b) reaches a

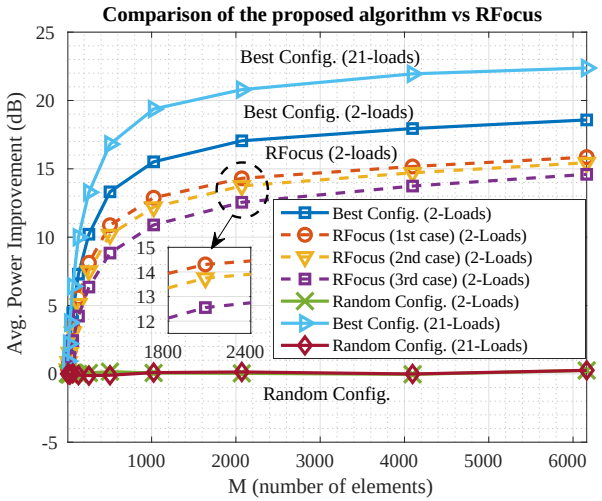

Fig. 10: Comparison of the proposed algorithm ("Best Config.") vs a majority voting algorithm [38].

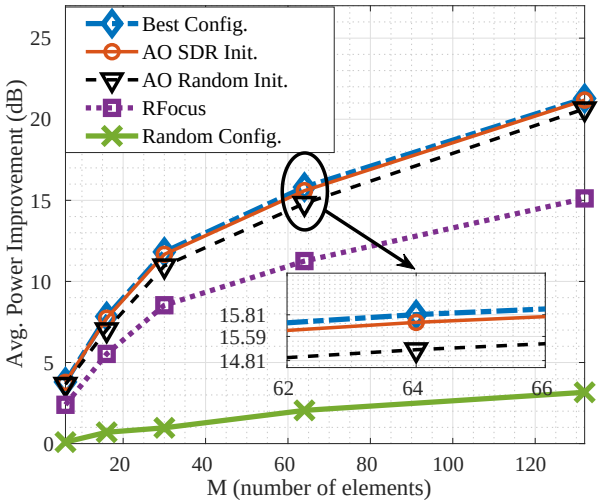

Fig. 11: Proposed algorithm ("Best Config.") vs suboptimal methods.

plateau with a faster rate than in (a), as a consequence of the larger element spacing. This finding suggests that even with perfect channel estimation, the weak nature of backscattered links limits the performance gains, even for large number of tags/RIS elements, in the order of $M = 6000$.

Fig. 10 shows a comparison of the average power improvement of the proposed algorithm versus a majority voting algorithm for $K = 2$ loads per RIS element, proposed in [38]. The distances are $d_{\text{RIS-SD}} = 1$ m, $d_{\text{SD}} = 3$ m and the element spacing is $d_x = \lambda/2$ and $d_y = \lambda/2$. Also, the transmission power is $P = 20$ dBm, $\eta = 10\%$ and $\kappa = 8$. The algorithm in [38] is feedback-based and uses K_r feedback measurements to decide which elements contribute constructively. Fig. 10 offers three cases: 1st case with $K_r = \left\lceil \frac{3(M+1)}{2} \right\rceil$, 2nd case with $K_r = M + 1$ and 3rd case with $K_r = \left\lceil \frac{M+1}{2} \right\rceil$, where M is the number of RIS elements. Parameter K_r was chosen proportionally to the total number of channels $M + 1$, with the underlying assumption that estimation of all channel coefficients in this work incurs a time overhead similar to the K_r feedback measurements. Fig. 10 shows that the proposed algorithm has a greater average power improvement for $K = 2$ loads. Also, it can further enhance its performance by using tags with $K > 2$ loads. In addition, the algorithm in [38] has a complexity of $O(MK_r)$ and it is required that $K_r \geq M$, so that a well-determined problem is crafted. The proposed algorithm is computationally more efficient, given that it has a complexity of $O(M \log M)$ compared to $O(MK_r)$, while it can efficiently find the optimal configuration even for $K > 2$ loads per RIS element. A specific example with $K = 21$ loads for the proposed algorithm is also depicted.

It is noted that both Figs. 9, 10 demonstrate that a quadratic scaling law of M^2 for the beamforming gain is not in place. This is not surprising, since as the number M of RIS elements increases, the distance of certain RIS elements from source or destination (of the SD link) also increases and hence, their contribution to the aggregate signal diminishes. The quadratic scaling law is valid only when the signal amplitude from each contributing element remains constant, as M increases, which is clearly not the case in realistic setups.

Fig. 11 presents a comparison between the proposed algorithm and state-of-the-art methods [38], [51], [52]. Alternative optimization (AO) with semi-definite relaxation-based initialization or random initialization are tested [51], [52]; with such AO, each element's estimated load is determined in an iterative manner, solving for each element separately, while fixing all the other elements' loads. Proper initialization of the elements' phase shifts is required. AO Random Init. depicts the performance of the AO algorithm with random initialization and the AO SDR Init. with quantization of the continuous phases obtained from [51], to the nearest discrete loads' phases. Perfect CSI is assumed with $\kappa = 3$, $v_{\text{X}} = 3$; moreover, $\eta = 10\%$, $d_0^{\text{X}} = d_{\text{SD}} = 3$ m, $f_2 = 870$ MHz, $P = 5$ dBm, and 20 dB relative end-2-end antenna gain for the backscattered links compared to direct link. Also, for the RFocus algorithm $K_r = M + 1$. All the algorithms depicted are for $K = 2$ loads of constant amplitude and difference in phase equal to π.

Based on Fig. 11 it is observed that the proposed algorithm outperforms both AO schemes and RFocus and provides the optimal solution. Furthermore, the SDR problem that initiates the loads of the AO SDR Init. has significant computational complexity in the number M of RIS elements of at least $O(M^{3.5})$ due to the utilized semi-definite relaxation, which is prohibitive for large intelligent surfaces (i.e., large M). That is why the figure is limited to a relatively small M, up to $M = 132$. In sharp contrast, the proposed algorithm conveniently scales up to a large number of elements M, in the order of hundreds to thousands, due to its attractive $O(M \log(M))$ computational complexity. Additionally, the formulation of [51] and [52] assumes a common constant amplitude reflection coefficient across all elements, which may not be the case in practical RIS designs and implementations. The proposed scheme is more general, since it can accommodate *any* set of

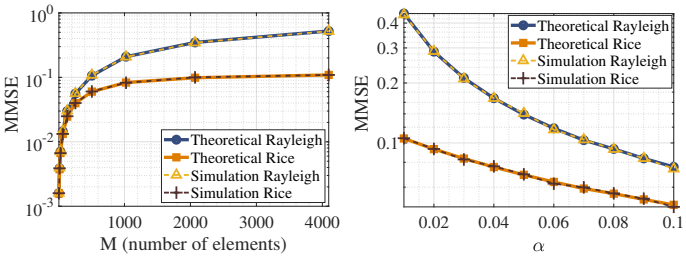

(a) MMSE vs M, $\alpha = 1\%$ (direct link present).

(b) MMSE vs α, $M = 4096$ (direct link present).

Fig. 12: MMSE vs M (a) and α (b), with RIS elements' spacing: $\frac{\lambda}{2}$.

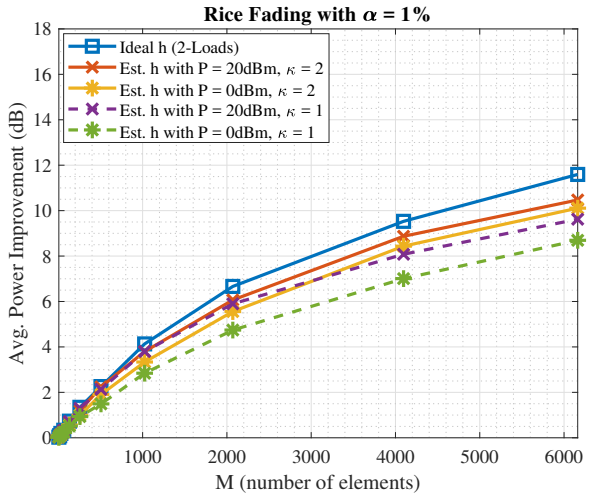

Fig. 13: Optimal Gain Performance vs M, with RIS elements' spacing: $\frac{\lambda}{2}$.

reflection coefficients, not necessarily of common amplitude.

Fig. 12 illustrates the LMMSE estimator's performance vs M (setup (a)) and vs percentage α of training symbols for channel estimation compared to the total number of symbols per coherence time (setup (b)). For both setups, $d_{\text{SD}} = 15$ m, $d_{\text{RIS-SD}} = 8$ m, $P = 20$ dBm, $\eta = 10\%$, $d_0^{\text{X}} = 3$ m and $v_{\text{X}} = 3$, while $\kappa = 15$ for Rice fading. Both figures demonstrate that simulation matches analysis results. As expected, an increase of M leads to an increased MMSE for fixed α, due to the corresponding reduction of training symbols available for the estimation of each h_m, $\forall m \in \{0, 1, , \ldots, M\}$. In addition, the Rice fading case outperforms the Rayleigh one, as a result of the inclusion of a much more powerful and deterministic LoS component in the Rice scenario, which leads to a significantly smaller variance regarding the values of h_m. Subsequently, after a few thousand RIS elements, the MMSE remains fixed at 10^{-1} in the Rice case. On the other hand, it is evident that as α increases the MMSE is reduced, while the differentiation between Rice and Rayleigh is prominent.

Fig. 13 depicts the optimal gain algorithm's performance, taking also into account CSI estimation, with Rice fading; various values of transmission power P and power ratio κ

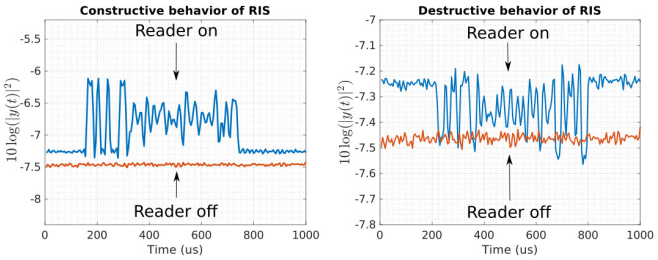

Fig. 14: Received signal strength at the destination: constructive vs destructive RIS impact.

are tested. The case of perfect (ideal) CSI estimation is also depicted, for comparison. For this setup it is assumed that $d_{\text{SD}} = 15$ m, $d_{\text{RIS-SD}} = 8$ m, $v_{\text{X}} = 3$, $d_0^{\text{X}} = 3$ m and $\eta = 10\%$. Since estimation error is inextricably related to SNR_m (where $\text{SNR}_m \propto P$), it is observed that for $P = 0$ dBm and $\kappa = 2$, the performance of the proposed algorithm drops, leading to a 2 dB difference compared to the ideal CSI case. The effect is even more evident when it is combined with a weak LoS, i.e. $\kappa = 1$, which yields a gain loss in the order of 3dB. It is further noted that these results assume $\alpha = 1\%$, which corresponds to a number of training symbols equal to 24×10^5, assuming channel coherence time equal to 100 msec and QPSK modulation at 48 Mbps. In less static, more mobile setups, where channel coherence time is much smaller, allocating such number of training symbols for channel estimation may not be a practical option.

B. Experiments with the Wireless, Batteryless Testbed

For the purposes of channel estimation, the reflective elements are required to terminate their antenna at loads attaining the values of A_s and 0 (as described in Sec. IV). Unfortunately, the commercial RFIDs we utilized as RIS elements do not support $\Gamma = A_s$. In addition, the exact loads of the RFID tag are not readily available. Thus, a different validation approach was adopted.

Fig. 14 offers the received power at the destination, operating @ 870 MHz, with the setup of Fig. 7 for two different configurations. With the reader on (@ 866 MHz), both the RIS and the SD link contribute to the received power (@ 870 MHz). With the reader switched off, the received power at the destination is measured and depicted. Clearly, one configuration offers constructive and another destructive RIS operation. The source-RIS distance was denoted as $d_{\text{RIS-S}}$ and the destination-RIS as $d_{\text{RIS-D}}$, measured from the RIS center; these parameters are the same as in Fig. 15.

Fig. 15 shows the maximum power improvement achieved as a function of number of configurations tested, for variable number of activated tags (denoted by μ). The setup corresponds to $d_{\text{RIS-S}} = 2.4$ m, $d_{\text{RIS-D}} = 1$ m and $d_{\text{SD}} = 2.1$ m. For a given configuration and μ, the value reported is over five repetitions. Increasing the number of configurations tested results to an increased maximum power value, on par with the simulation results. It is noted that the relatively small number of RIS elements/RFID tags tested, can only offer a small power

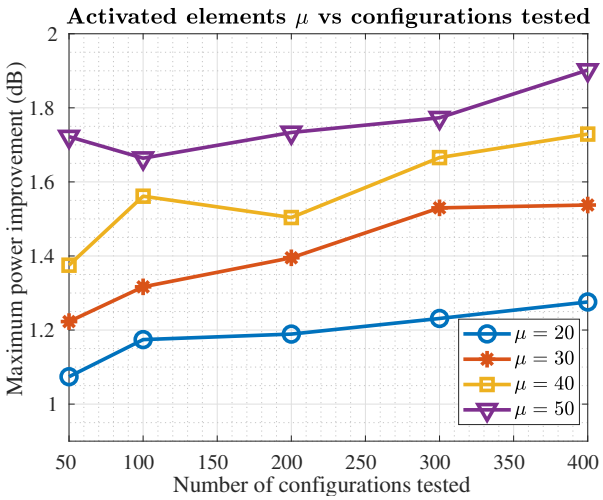

Fig. 15: Maximum power improvement vs Number of configurations tested for several μ.

TABLE I: Switching frequencies utilized by the backscattering tags.

Position \ d_X (m)	d_{SD}	d_{RIS-S}	d_{RIS-D}
1	2.10	3.22	1.09
2	2.24	3.18	1.09
3	3.25	4.02	1.09

improvement. Also, when μ is increased, the maximum gain is increased for a given number of configurations.

Fig. 17 offers the maximum power gain improvement, measured for three different source positions, over 1000 random configurations. For these experiments, a new RIS was established, consisting of $M = 256$ tags with $d_x = 5.25$ cm and $d_y = 5$ cm. The experiment was repeated for $\mu = \{64, 128, 192\}$ and for $P = \{0, 10\}$ dBm. The rest of the setup is kept static. Also, to reduce the amount of interference at the destination link, the reader was moved to 920 MHz. The individual distances for the three different source positions tested are listed in Table I and a schematic of the setup is depicted in Fig. 16. Results of these experiments are offered in Fig. 17.

Fig. 17 shows that the maximum gain improvement is highly associated with the position of the source link, since position 2 has the maximum gain for each value of μ. This leads to the conclusion that the channels have a dominant effect on the RIS operation and can either enhance or limit its performance. Also, increasing the number of effective tags μ is systematically improving the RIS performance, which shows that future applications should incorporate a higher number of tags (order of thousands) to achieve maximum gains. Additionally, varying the transmission power of the source P did not show any dramatic effect on the operation of the RIS.

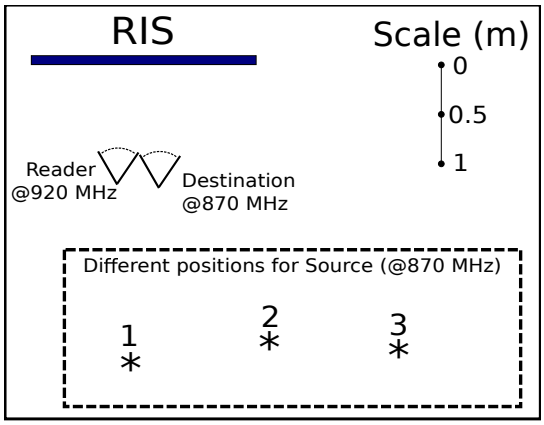

Fig. 16: Top view of the setup of Fig. 17.

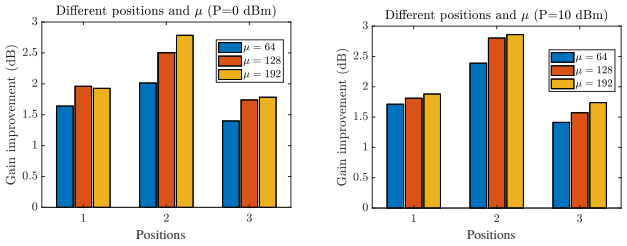

Fig. 17: Maximum power improvement for various positions and μ values ($P = \{0, 10\}$ dBm).

VII. Conclusion

It was shown that it is possible to find the optimal RIS element configuration with complexity of $O(M \log M)$, offering theory and results for large number M of RIS elements, in the order of thousands; in the latter case, complexity K^M of exhaustive search is prohibitive for any similar analysis. Comparison with prior art configuration also reveals the benefits of the proposed technique. It was also found that the passive nature of RIS, i.e., lack of amplification, limits the benefits, even for extended number of RIS elements. Channel estimation with LMMSE estimator is effective, provided that there are sufficient number of training/pilots symbols to estimate the compound channel for each of the $M + 1$ channel coefficients. For static environments with relatively long channel coherence time, that is possible; however, for mobile environments, such requirement may not be easy to satisfy. A wireless and batteryless testbed, designed with RFID tags was also demonstrated, pointing to the necessary modifications required, in order to wirelessly control the RFID tag/RIS elements. Future work could exploit findings of this work to offer a specialized protocol for more efficient wireless and batteryless RIS, using RFID and backscatter radio technology.

References

[1] C. Huang, S. Hu, G. C. Alexandropoulos, A. Zappone, C. Yuen, R. Zhang, M. D. Renzo, and M. Debbah, "Holographic MIMO Surfaces for 6G Wireless Networks: Opportunities, Challenges, and Trends," *IEEE Trans. Wireless Commun.*, vol. 27, no. 5, pp. 118–125, Oct. 2020.

[2] E. Björnson, Özgecan Özdogan, and E. G. Larsson, "Reconfigurable Intelligent Surfaces: Three Myths and Two Critical Questions," *IEEE Commun. Mag.*, vol. 58, no. 12, pp. 90–96, Dec. 2020.

[3] J. Kimionis, A. Bletsas, and J. N. Sahalos, "Bistatic backscatter radio for tag read-range extension," in *Proc. IEEE Int. Conf. on RFID-Technologies and Applications (RFID-TA)*, Nice, France, Nov. 2012.

[4] ——, "Bistatic backscatter radio for power-limited sensor networks," in *Proc. IEEE Global Commun. Conf. (Globecom)*, Atlanta, GA, Dec. 2013, pp. 353–358.

[5] ——, "Increased Range Bistatic Scatter Radio," *IEEE Trans. Commun.*, vol. 62, no. 3, pp. 1091–1104, Mar. 2014.

[6] P. N. Alevizos, K. Tountas, and A. Bletsas, "Multistatic scatter radio sensor networks for extended coverage," *IEEE Trans. Wireless Commun.*, vol. 17, no. 7, pp. 4522–4535, Jul. 2018.

[7] M. Ouroutzoglou, G. Vougioukas, G. N. Karystinos, and A. Bletsas, "Multistatic noncoherent linear complexity Miller sequence detection for Gen2 RFID/IoT," *IEEE Trans. Wireless Commun.*, vol. 20, no. 12, pp. 8067–8080, Dec. 2021.

[8] G. Vannucci, A. Bletsas, and D. Leigh, "A software-defined radio system for backscatter sensor networks," *IEEE Trans. Wireless Commun.*, vol. 7, no. 6, pp. 2170–2179, Jun. 2008.

[9] E. Kampianakis, J. Kimionis, K. Tountas, C. Konstantopoulos, E. Koutroulis, and A. Bletsas, "Wireless environmental sensor networking with analog scatter radio & timer principles," *IEEE Sensors J.*, vol. 14, no. 10, pp. 3365–3376, Oct. 2014.

[10] N. Fasarakis-Hilliard, P. N. Alevizos, and A. Bletsas, "Coherent detection and channel coding for bistatic scatter radio sensor networking," *IEEE Trans. Commun.*, vol. 63, pp. 1798–1810, May 2015.

[11] C. Konstantopoulos, E. Koutroulis, N. Mitianoudis, and A. Bletsas, "Converting a plant to a battery and wireless sensor with scatter radio and ultra-low cost," *IEEE Trans. Instrum. Meas.*, vol. 65, no. 2, pp. 388–398, Feb. 2016.

[12] S. N. Daskalakis, S. D. Assimonis, E. Kampianakis, and A. Bletsas, "Soil moisture scatter radio networking with low power," *IEEE Trans. Microwave Theory Tech.*, vol. 64, no. 7, pp. 2338–2346, Jul. 2016.

[13] P. N. Alevizos, A. Bletsas, and G. N. Karystinos, "Noncoherent short packet detection and decoding for scatter radio sensor networking," *IEEE Trans. Commun.*, vol. 65, no. 5, pp. 2128–2140, May 2017.

[14] G. Vougioukas, A. Dimitriou, A. Bletsas, and J. Sahalos, "Practical energy harvesting for batteryless ambient backscatter sensors," *Electronics*, vol. 7, no. 6, p. 95, Jun. 2018.

[15] G. Vougioukas and A. Bletsas, "Switching frequency techniques for universal ambient backscatter networking," *IEEE J. Select. Areas Commun.*, vol. 37, no. 2, pp. 464–477, Feb. 2019.

[16] V. Liu, A. Parks, V. Talla, S. Gollakota, D. Wetherall, and J. R. Smith, "Ambient backscatter: Wireless communication out of thin air," in *Proc. ACM SIGCOMM*, Hong Kong, China, 2013, pp. 39–50.

[17] A. Bletsas, P. N. Alevizos, and G. Vougioukas, "The art of signal processing in backscatter radio for μW (or less) internet of things: Intelligent signal processing and backscatter radio enabling batteryless connectivity," *IEEE Signal Processing Magazine*, vol. 35, no. 5, pp. 28–40, Sep. 2018.

[18] E. Bjrnson and L. Sanguinetti, "Power Scaling Laws and Near-Field Behaviors of Massive MIMO and Intelligent Reflecting Surfaces," *IEEE Open J. Commun. Soc.*, vol. 1, pp. 1306–1324, Sep. 2020.

[19] F. H. Danufane, M. D. Renzo, J. de Rosny, and S. Tretyakov, "On the Path-Loss of Reconfigurable Intelligent Surfaces: An Approach Based on Greens Theorem Applied to Vector Fields," *IEEE Trans. Commun.*, vol. 69, no. 8, pp. 5573–5592, Aug. 2021.

[20] C. Huang, A. Zappone, G. C. Alexandropoulos, M. Debbah, and C. Yuen, "Reconfigurable intelligent surfaces for energy efficiency in wireless communication," *IEEE Trans. Wireless Commun.*, vol. 18, no. 8, pp. 4157–4170, Aug. 2019.

[21] J. Lyu and R. Zhang, "Spatial throughput characterization for intelligent reflecting surface aided multiuser system," *IEEE Wireless Commun. Lett.*, vol. 9, no. 6, pp. 834–838, Jun. 2020.

[22] M. Di Renzo, F. Habibi Danufane, X. Xi, J. de Rosny, and S. Tretyakov, "Analytical modeling of the path-loss for reconfigurable intelligent surfaces anomalous mirror or scatterer ?" in *Proc. IEEE Workshop on Signal Process. Advances in Wireless Commun. (SPAWC)*, May 2020, pp. 1–5.

[23] W. Tang, M. Z. Chen, X. Chen, J. Y. Dai, Y. Han, M. Di Renzo, Y. Zeng, S. Jin, Q. Cheng, and T. J. Cui, "Wireless communications with reconfigurable intelligent surface: Path loss modeling and experimental measurement," *IEEE Trans. Wireless Commun.*, vol. 20, no. 1, pp. 421–439, Jan. 2021.

[24] M. Di Renzo, A. Zappone, M. Debbah, M.-S. Alouini, C. Yuen, J. de Rosny, and S. Tretyakov, "Smart radio environments empowered by reconfigurable intelligent surfaces: How it works, state of research, and the road ahead," *IEEE J. Select. Areas Commun.*, vol. 38, no. 11, pp. 2450–2525, Nov. 2020.

[25] M. A. Kishk and M. S. Alouini, "Exploiting randomly located blockages for large-scale deployment of intelligent surfaces," *IEEE J. Select. Areas Commun.*, vol. 39, no. 4, pp. 1043–1056, Apr. 2021.

[26] T. Bai and R. W. Heath, "Coverage and rate analysis for millimeter-wave cellular networks," *IEEE Trans. Wireless Commun.*, vol. 14, no. 2, pp. 1100–1114, Feb. 2015.

[27] L. Dai, B. Wang, Y. Yuan, S. Han, I. Chih-lin, and Z. Wang, "Non-orthogonal multiple access for 5G: solutions, challenges, opportunities, and future research trends," *IEEE Commun. Mag.*, vol. 53, no. 9, pp. 74–81, Sep. 2015.

[28] A. S. d. Sena, D. Carrillo, F. Fang, P. H. J. Nardelli, D. B. d. Costa, U. S. Dias, Z. Ding, C. B. Papadias, and W. Saad, "What role do intelligent reflecting surfaces play in multi-antenna non-orthogonal multiple access?" *IEEE Trans. Wireless Commun.*, vol. 27, no. 5, pp. 24–31, Oct. 2020.

[29] C. Zhang, W. Yi, and Y. Liu, "Reconfigurable intelligent surfaces aided multi-cell NOMA networks: A stochastic geometry model," Aug. 2020. [Online]. Available: http://arxiv.org/abs/2008.08457

[30] Y. Cheng, K. H. Li, Y. Liu, K. C. Teh, and H. Vincent Poor, "Downlink and uplink intelligent reflecting surface aided networks: NOMA and OMA," *IEEE Trans. Wireless Commun.*, vol. 20, no. 6, pp. 3988–4000, Jun. 2021.

[31] C. Liaskos, S. Nie, A. Tsioliaridou, A. Pitsillides, S. Ioannidis, and I. Akyildiz, "A new wireless communication paradigm through software-controlled metasurfaces," *IEEE Commun. Mag.*, vol. 56, no. 9, pp. 162–169, Sep. 2018.

[32] C. Liaskos, A. Tsioliaridou, A. Pitsillides, S. Ioannidis, and I. Akyildiz, "Using any surface to realize a new paradigm for wireless communications," *Commun. ACM*, vol. 61, no. 11, pp. 30–33, Oct. 2018.

[33] S. Abadal, C. Liaskos, A. Tsioliaridou, S. Ioannidis, A. Pitsillides, J. Sol-Pareta, E. Alarcn, and A. Cabellos-Aparicio, "Computing and communications for the software-defined metamaterial paradigm: A context analysis," *IEEE Access*, vol. 5, pp. 6225–6235, Apr. 2017.

[34] C. Liaskos, S. Nie, A. Tsioliaridou, A. Pitsillides, S. Ioannidis, and I. Akyildiz, "Realizing wireless communication through software-defined hypersurface environments," in *IEEE 19th International Symposium on "A World of Wireless, Mobile and Multimedia Networks" (WoWMoM)*, Jun. 2018, pp. 14–15.

[35] C. K. Liaskos, S. Nie, A. Tsioliaridou, A. Pitsillides, S. Ioannidis, and I. F. Akyildiz, "A novel communication paradigm for high capacity and security via programmable indoor wireless environments in next generation wireless systems," *Ad Hoc Networks*, vol. 87, pp. 1–16, 2019.

[36] Z. Li, Y. Xie, L. Shangguan, R. I. Zelaya, J. Gummeson, W. Hu, and K. Jamieson, "Towards Programming the Radio Environment with Large Arrays of Inexpensive Antennas," in *16th USENIX Symposium on Networked Systems Design and Implementation (NSDI 19)*, Boston, MA, Feb. 2019, pp. 285–300.

[37] L. Dai, B. Wang, M. Wang, X. Yang, J. Tan, S. Bi, S. Xu, F. Yang, Z. Chen, M. D. Renzo, and L. Hanzo, "Reconfigurable Intelligent Surface-Based Wireless Communications: Antenna Design, Prototyping, and Experimental Results," *IEEE Access*, vol. 8, pp. 45 913–45 923, Mar. 2020.

[38] V. Arun and H. Balakrishnan, "RFocus: Beamforming Using Thousands of Passive Antennas," in *17th USENIX Symposium on Networked Systems Design and Implementation (NSDI 20)*, Santa Clara, CA, Feb. 2020, pp. 1047–1061.

[39] W. Tang, J. Y. Dai, M. Z. Chen, K.-K. Wong, X. Li, X. Zhao, S. Jin, Q. Cheng, and T. J. Cui, "MIMO transmission through reconfigurable intelligent surface: System design, analysis, and implementation," *IEEE Trans. Commun.*, vol. 38, no. 11, pp. 2683–2699, Nov. 2020.

[40] A. Goldsmith, *Wireless Communications*. New York, NY, USA: Cambridge University Press, 2005.

[41] A. Bletsas, A. G. Dimitriou, and J. N. Sahalos, "Improving Backscatter Radio Tag Efficiency," *IEEE Trans. Microwave Theory Tech.*, vol. 58, no. 6, pp. 1502–1509, Jun. 2010.

[42] P. N. Alevizos, Y. Fountzoulas, G. N. Karystinos, and A. Bletsas, "Log-Linear-Complexity GLRT-Optimal Noncoherent Sequence Detection for Orthogonal and RFID-Oriented Modulations," *IEEE Trans. Commun.*, vol. 64, no. 4, pp. 1600–1612, Apr. 2016.

[43] Y. Zhang, K. Shen, S. Ren, X. Li, X. Chen, and Z.-Q. Luo, "Configuring intelligent reflecting surface with performance guarantees: Optimal beamforming," *IEEE J. Sel. Top. Signal Process.*, vol. 16, no. 5, pp. 967–979, Aug. 2022.

[44] G. Vougioukas, A. Bletsas, and J. N. Sahalos, "Instantaneous, Zero-Feedback Fading Mitigation with Simple Backscatter Radio Tags," *IEEE J. Radio Freq. Identif.*, Oct. 2020, early access.
[45] A. V. Oppenheim and G. C. Verghese, *Signals, Systems, and Inference*, ser. MIT 6.011 Course Note, 2010. [Online]. Available: https://ocw.mit.edu/courses/electrical-engineering-and-computer-science/6-011-introduction-to-communication-control-and-signal-processing-spring readings/MIT6_011S10_chap08.pdf
[46] S. Trampitch, "Complex-valued data estimation: Second-order statistics and widely linear estimators," Master's thesis, University of Klagenfurt, Apr. 2013.
[47] S. M. Kay, *Fundamentals of statistical signal processing. [Volume I]. , Estimation theory*. Upper Saddle River (N.J.): Prentice Hall, 1993.
[48] B. Hassibi and B. Hochwald, "How much training is needed in multiple-antenna wireless links?" *IEEE Trans. Inform. Theory*, vol. 49, no. 4, pp. 951–963, Apr. 2003.
[49] N. Kargas, F. Mavromatis, and A. Bletsas, "Fully-Coherent Reader With Commodity SDR for Gen2 FM0 and Computational RFID," *IEEE Wireless Commun. Lett.*, vol. 4, no. 6, pp. 617–620, Dec. 2015.
[50] Alien Technology LLC, "HIGGS-EC High Sensitivity RFID IC Datasheet," https://www.alientechnology.com/download/higgs-ec-files/?wpdmdl=7564&ind=QUxDLTM4MCBIaWdncy1FQyAyMDIwLTAyLTIxLnBkZg.
[51] Q. Wu and R. Zhang, "Intelligent Reflecting Surface Enhanced Wireless Network: Joint Active and Passive Beamforming Design," in *Proc. IEEE Global Commun. Conf. (Globecom)*, Dec. 2018, pp. 1–6.
[52] ——, "Beamforming Optimization for Intelligent Reflecting Surface with Discrete Phase Shifts," in *Proc. IEEE Int. Conf. Acoust. Speech Signal Process. (ICASSP)*, Mar. 2019, pp. 7830–7833.

Iosif Vardakis received the five-year Diploma and M.Sc. degrees in Electrical and Computer Engineering from the Technical University of Crete, Chania, Greece, in 2020 and 2022, respectively. His research interests include passive radar, signal processing for backscatter communication and satellite communications.

Georgios Kotridis received the five-year Diploma degree in Electrical and Computer Engineering from the Technical University of Crete (TUC), Greece, in 2021. His research interests lie on the areas of wireless communications, backscatter communications and signal processing.

Spyridon Peppas received the five-year Diploma degree in Electrical and Computer Engineering from the Technical University of Crete (TUC), Greece, in 2021. He is currently pursuing his Ph.D. degree at the University of Virginia (UVA), US, also in Electrical Engineering. His research interests include wireless communications, signal processing, optimization and machine learning.

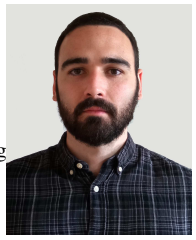

Konstantinos Skyvalakis received the five-year Diploma and M.Sc. degrees in electrical and computer engineering from the Technical University of Crete, Chania, Greece, in 2018 and 2021, respectively. His research interests include methods for low power wireless communications, signal processing for backscatter communication, satellite, and radar communications.

Georgios Vougioukas received the five-year Diploma degree and the PhD degree, in Electrical and Computer Engineering from Technical University of Crete (TUC), Greece, in 2016 and 2020, respectively. His research interests include methods for ultra-low power wireless communication, sensors, signal processing for backscatter communication, energy harvesting, analog & digital system design and implementation. He was the co-recipient of the 2017 IEEE International Conference on RFID Technology & Applications (RFID-TA) Best Student Paper Award, the second prize in the 2020 IEEE ComSoc Student Competition and the Best Paper award of the 2021 IEEE International Workshop on Wireless Communications and Networking in Extreme Environments (WCNEE).

Aggelos Bletsas (Senior Member, IEEE) received the Diploma degree (Hons.) in Electrical and Computer Engineering from the Aristotle University of Thessaloniki, Greece, in 1998, and the M.Sc. and Ph.D. degrees in Media Arts & Sciences from the Massachusetts Institute of Technology (MIT), Cambridge, MA, USA, in 2001 and 2005, respectively. He has worked with Mitsubishi Electric Research Laboratories (MERL), Cambridge, MA, USA and the RadioCommunications Laboratory (RCL), Department of Physics, Aristotle University of Thessaloniki, Greece. He currently serves as a Full Professor with the School of Electrical and Computer Engineering, Technical University of Crete, Greece. His research interests span the broad area of scalable wireless communications and sensor networking, with emphasis on ultra-low power/cost environmental sensing, backscatter radio & RFID, wireless localization and ambiently-powered inference networks. His current focus and contributions are relevant to wireless, batteryless, backscatter sensors for precision agriculture that cost a few Euros, consume a few microwatts and can be read with commodity receivers and smartphones. He has served as a Technical Program Committee (TPC) member for major IEEE conferences. He has served as an Associate Editor for IEEE TRANSACTIONS ON WIRELESS COMMUNICATIONS from 2015 to 2021 and IEEE WIRELESS COMMUNICATIONS LETTERS from 2011 to 2016. Since June 2022 he is serving as Area Editor for IEEE TRANSACTIONS ON WIRELESS COMMUNICATIONS. He was co-recipient of the IEEE Communications Society 2008 Marconi Prize Paper Award in Wireless Communications, and various Best (Student) Paper Awards, e.g., in IEEE RFID-TA 2011, IEEE ICASSP 2015, IEEE RFID-TA 2017, MOCAST 2018 and IEEE WCNEE 2021. Prof. Bletsas received the 2012-2013 Technical Univ. of Crete Research Excellence Award. In December 2020, his students won the Second Prize in the 2020 IEEE ComSoc "Communications Technology Changing the World" Student Competition. He is also proud of his students who were winners for two consecutive years of the 2009-2011 and 2011-2012 best Diploma Thesis contest among all Greek Universities on "Advanced Wireless Systems", awarded by IEEE VTS/AES joint Greek Chapter. He is regularly listed in the Top 2% Scientists worldwide annual list compiled by Prof. Ioannidis group at Stanford Univ. and has been included in the Highly Cited Greek Scientists, as well as 45 Highly Cited Greek Scientists under 45 list. One of his articles is ranked 1st in Google Scholar Classic Papers in Computer Networks and Wireless Communication.